# Two-dimensional confinement of excitons at the interface in nonpolar MgZnO/ZnO heterostructures

Muhammad Zakria, David J Rogers, Joseph Scola, Liangchen Zhu, Mark Lockrey, Philippe Bove, Eric V Sandana, Ferechteh H Teherani, Matthew R Phillips, Cuong Ton-That

# Two-dimensional confinement of excitons at the interface in nonpolar MgZnO/ZnO heterostructures

Muhammad Zakria,[1] David J. Rogers,[2] Joseph Scola,[3] Liangchen Zhu,[1] Mark Lockrey,[1] Philippe Bove,[2] Eric V. Sandana,[2] Ferechteh H. Teherani,[2] Matthew R. Phillips,[1] and Cuong Ton-That[1,*]

[1]*School of Mathematical and Physical Sciences, University of Technology Sydney, Ultimo, New South Wales 2007, Australia*

[2]*Nanovation, 8 Route de Chevreuse, 78117 Châteaufort, France*

[3]*Groupe d'Étude de la Matière Condensée, UMR 8635 CNRS, 45 avenue des Etats-Unis, 78035 Versailles Cedex, France*

(Received 30 September 2021; accepted 22 February 2022; published 15 March 2022)

We report on the polarity-dependent excitonic emission at the interface in MgZnO/ZnO heterostructures grown on both polar and nonpolar ZnO single-crystal substrates. Structural and morphological analyses confirm that the heterostructures grow homoepitaxially on nonpolar *m*-plane and *a*-plane crystal substrates. The nonpolar heterostructures are investigated by depth-resolved cathodoluminescence spectroscopy revealing an excitonic interface emission centered at 3.12 eV, identified as the *H*-band signature of indirect excitons. These results reveal the formation of robust indirect excitons confined at the MgZnO/ZnO interface due to the presence of an epitaxially strained interfacial layer near the interface in the MgZnO, which is confirmed by high-order x-ray diffraction. It is also found that the *H*-band emission originates from the self-absorption of the ZnO free exciton emission in the proximity of the interface. Temperature-dependent studies of the *H* band yields a thermal activation energy of 47 meV for the indirect exciton in the nonpolar heterojunctions. This activation energy is the largest among all free and bound excitons in ZnO and is much higher than the values found in AlGaN/GaN and MgZnO/ZnO/sapphire hetrostructures. Our findings indicate that the optical properties of nonpolar heterostructures are strongly influenced by the piezoelectric effect.

DOI: 10.1103/PhysRevMaterials.6.035202

## I. INTRODUCTION

The possibility of forming two-dimensional (2D) electron or hole gases and associated excitons at the interfaces in wide band-gap heterostructures, such as MgZnO/ZnO and AlGaN/GaN, has great potential in high-frequency and high power device applications [1–4]. Moreover, a recent breakthrough has been reported for a GaN/AlN heterointerface in which a comparatively high 2D hole gas density exists without the need for acceptor doping [1]. Compared with GaN-based heterostructures, the MgZnO/ZnO system has several merits, including larger spontaneous polarization fields ($P_{ZnO} = -0.057$ and $P_{GaN} = -0.029\,C/m^2$), and smaller lattice mismatch for the same conduction-band offset [5,6]. Furthermore, as ZnO has a larger exciton binding energy (60 meV) and a small electron effective mass, there has been an immense interest in its use in exciton-based optical applications [7]. As a result, ZnO has been extensively studied for use in light-emitting diodes, lasers, photodetectors, and piezoelectronic devices [7–9]. To date, studies of excitons localized at the interface in ZnO/MgZnO heterostructures have focused on layers grown on *c*-plane polar substrates and their association with the broken symmetry along the polar axis of the wurtzite crystal structure. Here, we report the formation of robust excitons confined at the 2D interface of nonpolar MgZnO/ZnO heterostructures, which can be attributed entirely to internal piezoelectric polarization fields at the interface. The 2D exciton confinement in nonpolar heterostructures and bound charges at the interface is shown to strongly influence the optical and electrical properties of oxide devices based on nonpolar materials.

Wurtzite (Mg,Zn)O has a noncentrosymmetric crystallographic structure with a relatively strong built-in spontaneous polarization. Layers and quantum well (QW) structures with the orientation along the energetically favorable *c*-axis growth direction exhibit a spontaneous polarization. This internal electric field can have detrimental effects, such as lowering the probability of radiative recombination due to the spatial separation of electrons and holes, known as the quantum-confinement Stark effect [10]. Growing QW structures epitaxially on nonpolar substrates (i.e., nonequilibrium crystallographic orientations) annuls this, and such structures have been shown to exhibit higher emission intensity as well as polarized photoluminescence as a result of strain-induced modifications of electronic bands [11–14]. Hence, device structures based on nonpolar substrates, especially *a*-plane (11-20) and *m*-plane (10–10) sapphire, have been utilized in photodiodes, photodetectors, and transistors [11,15]. In theory, nonpolar ZnO substrates offer a much better platform for ZnO/MgZnO interface studies than sapphire because the native substrates have no lattice or thermal mismatch with the epilayers. Thus, we can expect zero spontaneous polarization field in the growth direction. However, studies of epitaxially grown heterostructures on nonpolar ZnO crystals are scarce. This can be attributed to two factors: (i) A variable quality of polishing, which can negatively impact the quality of the crystal surface and (ii) the comparatively high

*cuong.ton-that@uts.edu.au

 

growth temperatures which are commonly used for ZnO epitaxy can provoke a degradation of the surface morphology. Both issues have a strong impact on the interface optical emission and have hampered the adoption of ZnO substrates in fundamental studies. In this paper, a proprietary chemical mechanical polishing (CMP) method was employed in order to minimize both surface roughness and subsurface damage. MgZnO/ZnO heterostructures were then simultaneously grown on polar *c*-plane and nonpolar *m*- and *a*-plane ZnO substrates using pulsed laser deposition (PLD). PLD offers the advantage of plasma-enhanced adatom mobilities which facilitates high-quality epitaxy at reduced substrate temperatures compared to thermal growth techniques, such as molecular beam epitaxy or metal organic chemical vapor deposition [16]. These reduced substrate temperatures suppress the substrate morphology degradation that has been observed at higher growth temperatures by inhibiting the diffusion of subsurface polishing damage to the substrate surface [17].

## II. EXPERIMENTAL DETAILS

Polar (*c*-plane) and nonpolar (*a*- and *m*-plane) ZnO substrates (size $5 \times 5 \times 0.5\,\mathrm{mm}^3$) were cut from hydrothermal single-crystal wafers prepared by Materials, Inc. The substrates were annealed at 1100 °C in oxygen for 1 h in order to drive Li and other group-I impurities to the surface [18]. These impurities were subsequently removed using CMP at NOVASiC so as to prepare the epi-ready surface for epitaxial growth. ZnO epilayers were grown by PLD using a sintered 5N ZnO powder target with a Coherent LPX 100 KrF (248 nm) excimer laser. MgZnO layers were grown, subsequently, using a sintered 5N MgZnO (13.4 at. % Mg) target under an oxygen pressure of $5 \times 10^{-4}$ Torr as described previously [19]. The crystal substrate was kept at 500 °C during the growth. The layer thicknesses were 15 and 360 nm for MgZnO and ZnO, respectively. High-resolution x-ray diffraction (HR-XRD) was performed in a Panalytical MRD Pro system using Cu $K\alpha_1$ radiation. Morphological investigations were conducted using a field emission scanning electron microscope (SEM) (Thermo Scientific Helios G4 DualBeam) operating at 10 kV. Temperature-dependent Hall measurements were carried out using a Van der Pauw configuration with indium contacts at the four corners of the sample. Cathodoluminescence (CL) microanalysis of the films was conducted in an FEI Quanta 200 Environmental SEM equipped with a diamond-machined parabolic light collector and a Hamamatsu S7011-1007 CCD spectrometer. In depth-resolved CL measurements, the accelerating voltage was systematically varied between 2 and 12 kV whereas the electron-beam (e-beam) current was adjusted at each voltage so that the beam power was kept constant at 25 $\mu$W. In this way, CL data acquired at different depths could be directly compared as the number of generated electron-hole pairs at each measurement voltage remained constant [20]. The oxide samples were found to be highly stable; no e-beam induced changes to the CL emission were detected under the excitation conditions used in this work.

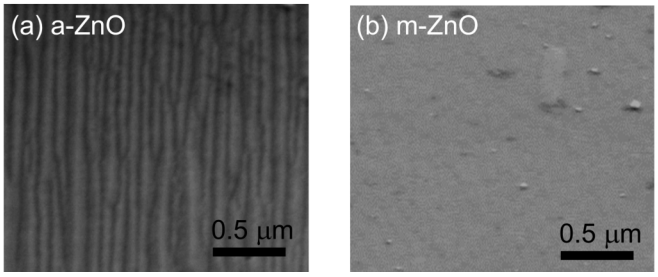


FIG. 1. SEM images of the MgZnO/ZnO homoepitaxial heterostructures grown on nonpolar *a*- and *m*-plane ZnO crystal substrates.

## III. RESULTS AND DISCUSSION

### A. Structural properties of homoepitaxial MgZnO/ZnO heterostructures grown on nonpolar ZnO substrates

Figure 1 presents SEM images of the MgZnO/ZnO heterostructures grown on the nonpolar *a*- and *m*-ZnO single crystals. For the heterostructure grown on *a*-ZnO, the surface shows a corrugated morphology with parallel ridges running vertically, similar to those observed by scanning tunneling microscopy for ZnO epilayers grown on *a*-plane ZnO surfaces [21]. These ridges were shown to run along the $[\bar{1}100]$ direction with facets limited by $\pm(0001)$ planes [21]. The MgZnO/ZnO heterostructure grown on the *m*-plane ZnO, on the other hand, exhibits a smoother surface with occasional rhombohedral islands; such morphology is commonly observed in the growth of nonpolar ZnO films as they preferentially grow laterally along the *c*-axis orientation [22,23]. Hall effect measurements gave carrier densities in the range of $2 \times 10^{18}$–$6 \times 10^{18}\,\mathrm{cm}^{-3}$, which was attributed to the heterostructures because the substrates were significantly more insulating. The mobilities at 300 K for the heterostructures on the nonpolar substrates were exceptionally high ($\mu_{a\,\mathrm{plane}} = 600\,\mathrm{cm}^2/\mathrm{Vs}$ and $\mu_{m\,\mathrm{plane}} = 750\,\mathrm{cm}^2/\mathrm{Vs}$) and significantly larger than that for the polar counterpart ($\mu_{c\,\mathrm{plane}} = 300\,\mathrm{cm}^2/\mathrm{Vs}$). All the heterostructures (on the *c*-, *a*- and *m*-ZnO crystal substrates) exhibited monotonic decreases in carrier mobility with decreasing temperature (see the Supplemental Material Fig. 1S [24]) in a similar manner to a comparable reference bilayer grown on a sapphire substrate, which could be explained by interface roughness scattering [3].

The epitaxial growth of the MgZnO/ZnO bilayers on the crystal substrates and their *d* spacings were evaluated by HR-XRD. Figures 2 and Supplemental Material Fig. 2S [24] show HR-XRD $2\theta/\Omega$ scans for the MgZnO/ZnO bilayers and corresponding ZnO crystal substrates, revealing that the MgZnO/ZnO bilayers grow epitaxially on the respective ZnO substrates. All the substrates and bilayers show peaks indicative of single phase wurtzite structure and the *d* spacing of the ZnO layer is exactly as would be expected for wurtzite ZnO (according to the JCPDS 36–1451 reference). The MgZnO peak is situated on the left side of the main ZnO peak for all the bilayers. The piezoelectric polarization is sensitive to the strain state of the MgZnO overlayer, which is analyzed by reciprocal space mapping (RSM). The RSMs recorded around

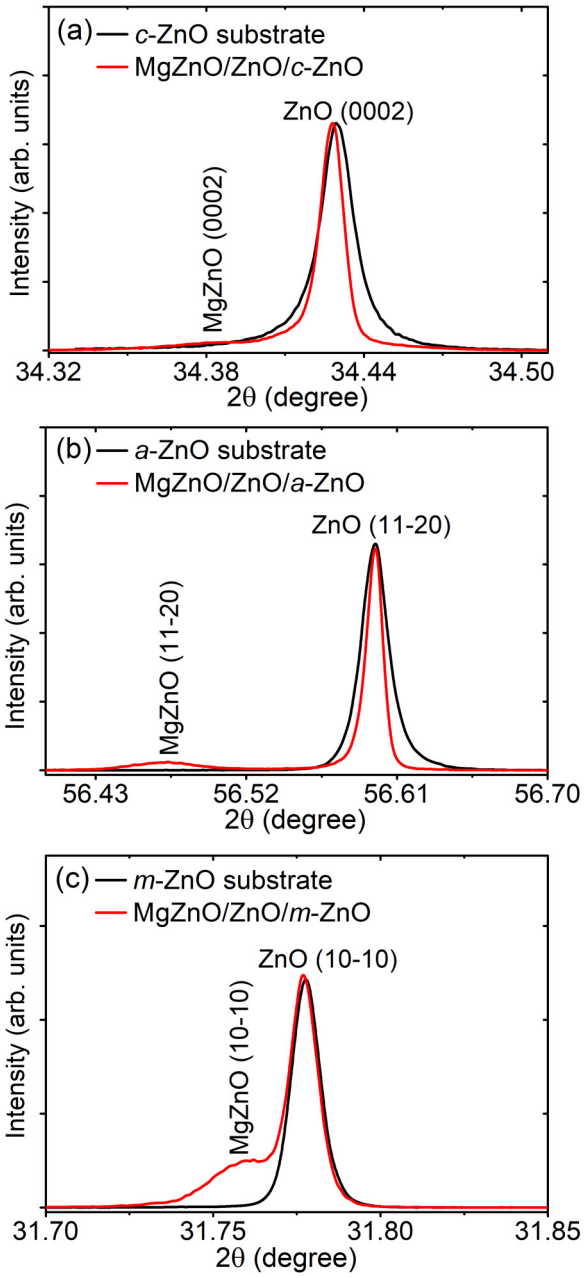


FIG. 2. Normalized HR-XRD $2\theta/\Omega$ scans for the main peaks of the MgZnO/ZnO bilayers grown on the *c*-, *a*-, and *m*-plane ZnO crystal substrates. The XRD patterns show peaks indicative of the single-phase wurtzite structure. For all the bilayers, the peak of the ZnO layer is comparable in position to the bulk substrate, and the MgZnO peak is situated on the left side of the main ZnO peak.

the main reflection for each of the MgZnO/ZnO bilayers are presented in Fig. 3S of the Supplemental Material [24]. The RSMs reveal that the ZnMgO layers are not fully relaxed for the nonpolar ZnO substrates. A small third peak, related to the growth of the MgZnO layer, appears at a higher value of $q_\perp$ than the ZnO layer for the bilayers on the *a*- and *m*-ZnO substrates. This peak arising from an epitaxially strained thin layer in the MgZnO is more evident in the high-order Bragg reflections shown in Supplemental Material Fig. 4S [24]. These XRD profiles are fitted with Voigt functions with the two main components corresponding to the reflections from ZnO and MgZnO layers. There exists a third peak in the bilayers on the nonpolar *a*- and *m*-ZnO substrates, which can be ascribed to a thin interfacial layer formed to accommodate the substrate strain. From the diffraction intensities, this interfacial layer was estimated to be <2 nm in thickness. The *d* spacings corresponding to the XRD peak positions of the ZnO and MgZnO layers as well as the interfacial layer are shown in Table 1S of the Supplemental Material [24]. The MgZnO layers on the *c*-, *a*-, and *m*-plane crystal substrates exhibit *d* spacings of 2.606, 1.628, and 2.815 Å, respectively, which are slightly larger than the values found for the respective ZnO underlayers (2.604, 1.625, and 2.811 Å). This is consistent with larger $Mg^{2+}$ ions substituting for $Zn^{2+}$ ions in the MgZnO overlayer. The *d* spacing of the interfacial layer is smaller than that of the MgZnO layer, indicating that it is compressively strained by the ZnO underlayer.

### B. Excitation of the *H* band by free excitons

Depth-resolved CL measurements were conducted on the single ZnO layers and the corresponding MgZnO/ZnO heterostructures on the *a*-, *m*-, and *c*-plane crystal substrates to establish the origin of the interface-bound emission. The CL emission at the heterointerface is assigned to an *H*-band emission based on comparison of the CL spectra of the

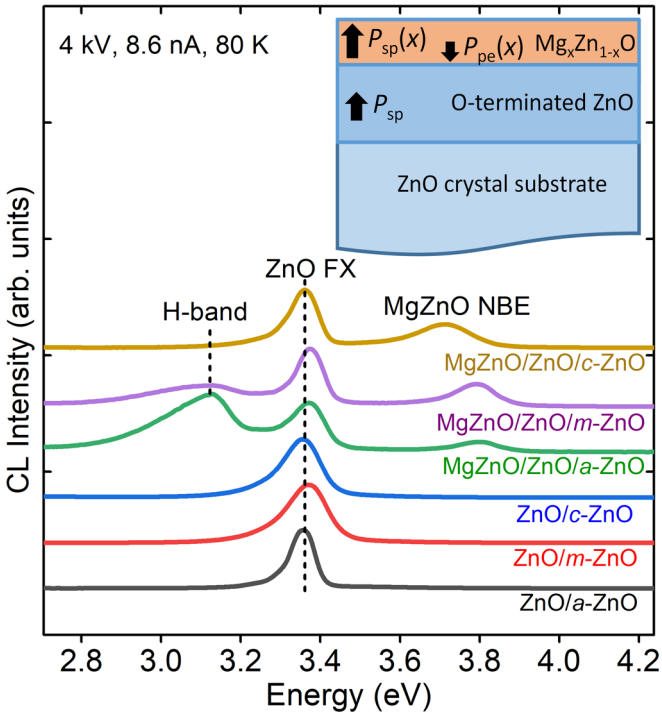


FIG. 3. CL spectra at 80 K for the ZnO layers and MgZnO/ZnO heterostructures grown on *a*-, *m*-, and *c*-plane ZnO single-crystal substrates. All the spectra are dominated by the ZnO FX emission at 3.37 eV. The heterostructures on the nonpolar *a*- and *m*-ZnO substrates exhibit a luminescent *H* band at 3.12 eV, which is absent in the constituent ZnO underlayer as well as in the heterostructure on the *c*-ZnO substrate. The inset shows the distribution of polarization fields for the heterostructure on the *c*-ZnO substrate. $P_{sp}$ and $P_{pe}$ represent the spontaneous and piezoelectric polarizations, respectively.

heterostructures with those of the reference ZnO underlayers (i.e., without a MgZnO overlayer). *H*-band luminescence is produced by the radiative recombination of indirect excitons formed by a 2D electron in the triangular quantum well at the MgZnO/ZnO interface with a hole in the near-interface ZnO region [3,25]. Figure 3 shows the CL spectra for the ZnO layers and the MgZnO/ZnO heterostructures for an acceleration voltage of 4 kV, corresponding to an excitation depth of 110 nm. The CL spectra for all the ZnO layers consist of a dominant peak at 3.37 eV, attributable to free exciton (FX) transition in ZnO with a low-energy optical sideband due to exciton-longitudinal-optical (LO) phonon coupling. The spectra for the heterostructures on the nonpolar *a*- and *m*-ZnO exhibit three peaks: a ZnO FX emission at 3.37 eV, a near-band-edge (NBE) emission of the MgZnO overlayer at ∼3.8 eV, and a broad peak at 3.12 eV labeled as the *H* band. The term *H* band has frequently used to describe to an optical emission arising from heterojunctions of nitrides, arsenides, and oxides [26]. The NBE emission of the MgZnO on the nonpolar ZnO at 3.8 eV corresponds to a Mg concentration of 24 at.% [27]. It is worth noting that the determination of the Mg concentration using the NBE emission energy of the MgZnO is more reliable than using the XRD *d* spacings due to the epitaxial strain state of the MgZnO overlayer. The MgZnO layer grown on the *c*-ZnO substrate exhibits a lower NBE emission energy (3.7 eV), compared with those on the nonpolar substrates, which indicates a lower Mg composition in the MgZnO alloy. Lower Mg concentration in the MgZnO layer results in smaller band offsets and a reduced polarization field, which might contribute to the absence of *H* band in the MgZnO/ZnO/*c*-ZnO structure. The *H* band is not detected in any of the ZnO underlayers, and, thus, it is taken that the *H* band originates from the MgZnO/ZnO interface. The *H*-band emission is most intense in the MgZnO/ZnO/*a*-ZnO heterostructure and negligibly weak in the MgZnO/ZnO/*c*-ZnO heterostructure.

The distribution of polarization fields for the heterostructures can be depicted schematically in the inset of Fig. 3. $P_{sp}$ represents the spontaneous polarizations and $P_{pe}(x)$ is the piezoelectric polarization arising from the crystallographically strained $Mg_xZn_{1-x}O$ layer. In the *c*-plane MgZnO/ZnO bilayer, both $P_{sp}$ and $P_{pe}$ are present, thus, the total polarization is $[P_{sp}(x)–P_{sp}]–P_{pe}(x)$. The negligibly weak *H* band in the heterostructure on the *c*-ZnO substrate suggests the

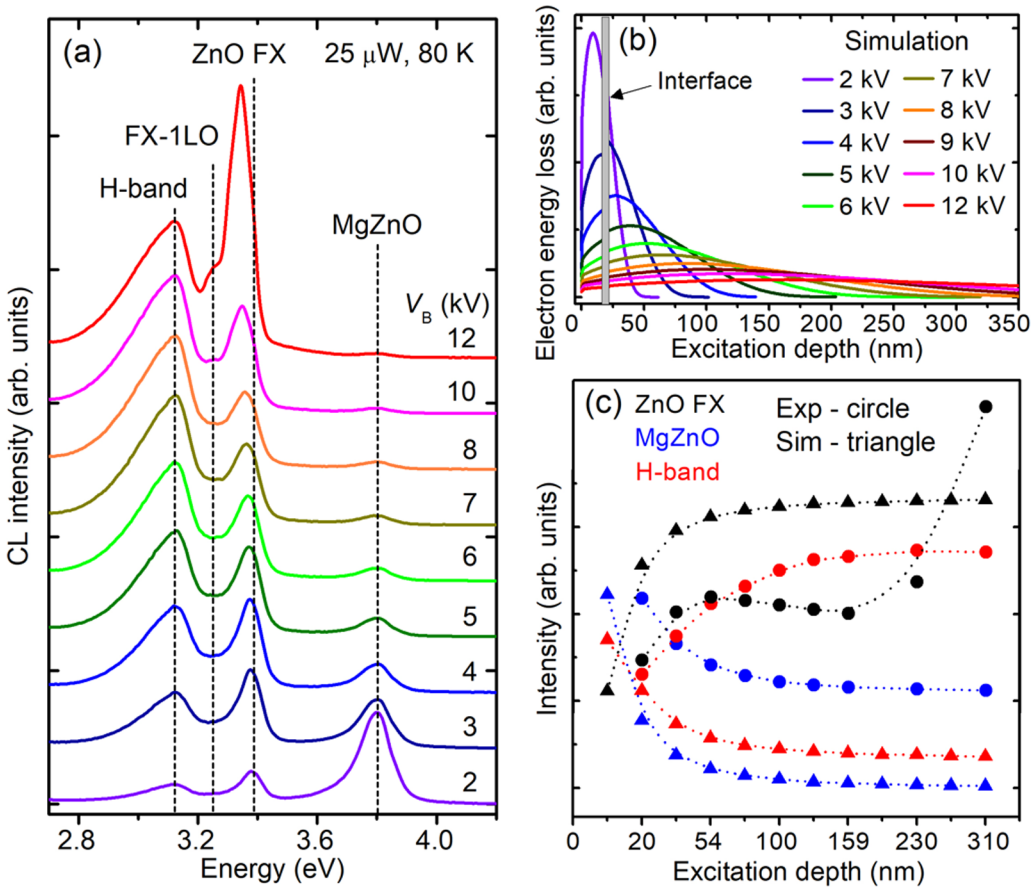


FIG. 4. (a) Depth-resolved CL spectra of the MgZnO/ZnO heterostructure on the *a*-ZnO substrate acquired at acceleration voltages between 2 and 12 kV. The *H* band increases monotonically with acceleration voltage even when almost all carriers are injected into the ZnO underlayer, whereas the MgZnO NBE decreases in intensity as expected. (b) Simulated electron-loss curves for the MgZnO/ZnO heterostructure for acceleration voltages between 2 and 12 kV. (c) Integrated intensities of the ZnO FX, *H* band, and MgZnO NBE together with their simulated emission intensities, plotted as functions of excitation depth over the 2–12-kV voltage range. The experimental and simulated CL depth profiles for MgZnO and ZnO FX are consistent, whereas the experimental and modeled H-band profiles are in complete disagreement due to self-absorption of the FX emission by ZnO in the region near the MgZnO/ZnO interface.

compensation of spontaneous polarization by the piezoelectric field. This finding is similar to the negligible internal electric field observed in QW structures with well widths below 4.6 nm [28]. For the nonpolar ($a$- and $m$-plane) bilayers, the spontaneous polarization fields can be neglected, and, hence, the total polarization simply becomes $-P_{pe}(x)$. The strong $H$ band in the nonpolar MgZnO/ZnO heterostructures is consistent with the presence of the compressively strained interfacial layer in the MgZnO as demonstrated above.

To investigate the origin of the $H$-band luminescence, depth-resolved CL was conducted on the MgZnO/ZnO/$a$-ZnO heterostructure. Figure 4(a) shows the CL spectra for acceleration voltages between 2 and 12 kV, corresponding to an excitation depth of 20–310 nm under a constant excitation power of 25 $\mu$W. These spectra reveal that: (i) the heterostructure exhibits all three emission bands throughout this range of excitation depths, (ii) as the excitation depth is increased both the FX and the $H$-band peaks become stronger whereas the MgZnO NBE decreases in intensity, and (iii) the enhanced FX emission above 8 kV where the beam excites the ZnO crystal substrate, arises due to a lower concentration of nonradiative defects in the bulk crystal substrate compared with the PLD epilayer. To investigate the depth-dependent properties of the $H$ band, the in-depth and in-plane profiles of the electron energy loss (EEL) in the heterostructure were modeled for each kV through a "CASINO" Monte Carlo simulation [29]. The electron energy-loss curves reveal the spatial distribution of the injected electron hole pairs and the corresponding CL intensity. Figure 4(b) shows the in-depth energy-loss profiles of electrons in the MgZnO/ZnO heterostructure for acceleration voltages between 2 and 12 kV. At the lowest voltage (2 kV) injected electrons begin to be deposited into the interface region, resulting in a relatively strong $H$-band emission. Intriguingly, the $H$-band emission continues to rise with increasing excitation depth when almost all electrons are injected into the ZnO underlayer at acceleration voltages of $>4$ kV. The simulated EEL profiles shown in Fig. 4(b) are integrated over each layer to model the peak intensity for the ZnO FX, $H$ band and MgZnO emissions at each kV. For the $H$ band, an arbitrary thickness of 8 nm (4 nm above and 4 nm below the MgZnO/ZnO interface) was used. To verify the 2D nature of the $H$-band exciton, we plot integrated intensities of the ZnO FX, $H$ band, and MgZnO NBE together with their simulated emission intensities as functions of excitation depth [Fig. 4(c)]. The experimental $H$-band in-depth profile has a completely different shape to those of both ZnO and MgZnO, which confirms that the $H$-band emission does not arise from the ZnO or MgZnO layer. The MgZnO and ZnO in-depth profiles from the experimental and simulated results are consistent in shape, whereas the experimental and modeled $H$-band profiles show opposite trends with increasing excitation depth (rising and decreasing, respectively). A highly plausible explanation for the $H$-band behavior is that the ZnO FX emission is self-absorbed near the interface by the ZnO epilayer. Here, the FX absorption excites additional carriers in the proximity of the MgZnO/ZnO interface region, producing a greater

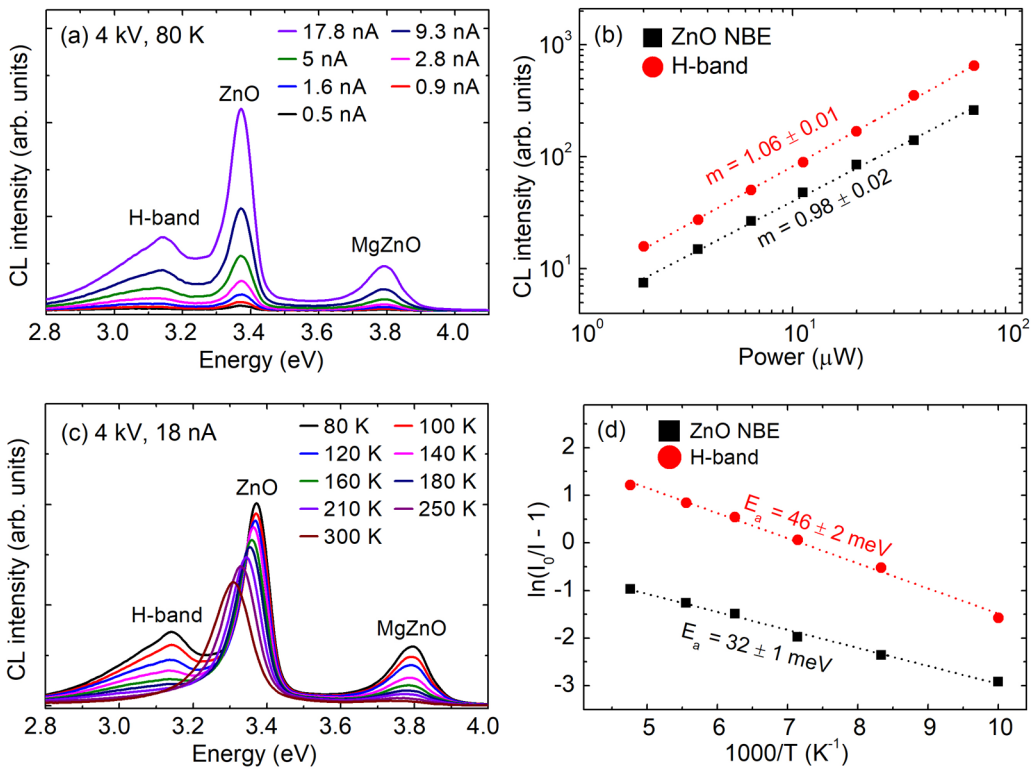


FIG. 5. (a) Excitation power-resolved CL spectra for the MgZnO/ZnO/$m$-ZnO heterostructure ($V_B = 4$ kV, $I_B = 0.5$–17.8 nA). (b) Analysis of the integrated peak intensities of the $H$ band and ZnO NBE using the power-law model, showing linear relationships with excitation power. (c) Temperature-resolved CL spectra for the MgZnO/ZnO/$m$-ZnO, showing the presence of the H-band emission at temperatures up to 250 K. (d) Activation energies for the $H$ band and ZnO NBE emission determined using the Arrhenius law: $E_a$($m$-ZnO) $= 32 \pm 1$ and $E_a$($H$ band) $= 46 \pm 2$ meV.

number of interface localized indirect excitons and, as a result, an increase in the observed $H$-band intensity. Significantly, the $H$-band emission intensity relative to the FX is found to be strongest when free excitons in ZnO are generated within 120 nm from the interface; this value corresponds to the expected carrier recombination length in the ZnO epilayer. This $H$-band enhancement model is supported by the observed redshift of the ZnO FX peak up to 40 meV with increasing excitation depth [see Fig. 4(a)], which originates from the strong self-absorption of the high-energy side of the FX peak by the ZnO region below the interface. Such optical absorption excites additional carriers, which migrate towards the notch potential well at the interface [3], producing a great number of bound interface excitons and a strong $H$-band emission. The simulation results for the MgZnO/ZnO heterostructure in Fig. 4(c) show that the e-beam generated $H$-band component decreases with rising excitation depth, whereas the FX generated contribution to the $H$ band continues to rise with increasing FX intensity over the 2–12-kV beam voltage range. The combination of these two effects produces the observed initial increase and flattening of the $H$ band with increasing excitation depth as shown in Fig. 4(c) and confirms that the measured $H$-band intensity profile is totally consistent with the self-absorption model. With increasing excitation depth above 120 nm from the interface, the elevated ZnO FX emission does not produce a corresponding increase in the $H$-band intensity because the energy of the FX emission falls below the ZnO band gap as a result of the self-absorption effect. These results confirm the excitation of the $H$ band by the absorption of the ZnO FX emission.

### C. Thermal activation energy of the $H$ band

Given the coupling mechanism of the ZnO FX and the $H$ band, it is expected that these two emissions show similar excitation power dependencies. The excitation power- and temperature-resolved CL results for the heterostructure on the nonpolar $a$- and $m$-ZnO substrates are presented in Figs. 5 and 6, respectively. These figures show no changes in peak position and shape for the ZnO FX and MgZnO NBE peaks with increasing excitation power at 80 K, which reflects the excitonic nature of these emissions and negligible exciton-exciton scattering effects. There is no observed shift of the $H$-band emission with increasing excitation intensity under the CL conditions employed, which can be explained as being due to only a small fraction of injected carriers being excited in the interface region [see Fig. 4(b)]. The power-dependent characteristics of the $H$-band intensity are further analyzed using a power-law model, $I_{CL} \propto I_B{}^m$, where $I_{CL}$ is the integrated CL intensity and $I_B$ is the e-beam current [Figs. 5(b) and 6(b)]. The logarithmic plot gives the exponent $m$ to be between 0.91 and 1.06 for both the ZnO FX and $H$-band emissions. Defect-related emissions in ZnO have previously been shown to exhibit sublinear dependence on the excitation power [30]; the $H$-band emissions observed in both nonpolar MgZnO/ZnO heterostructures do not display such behavior,

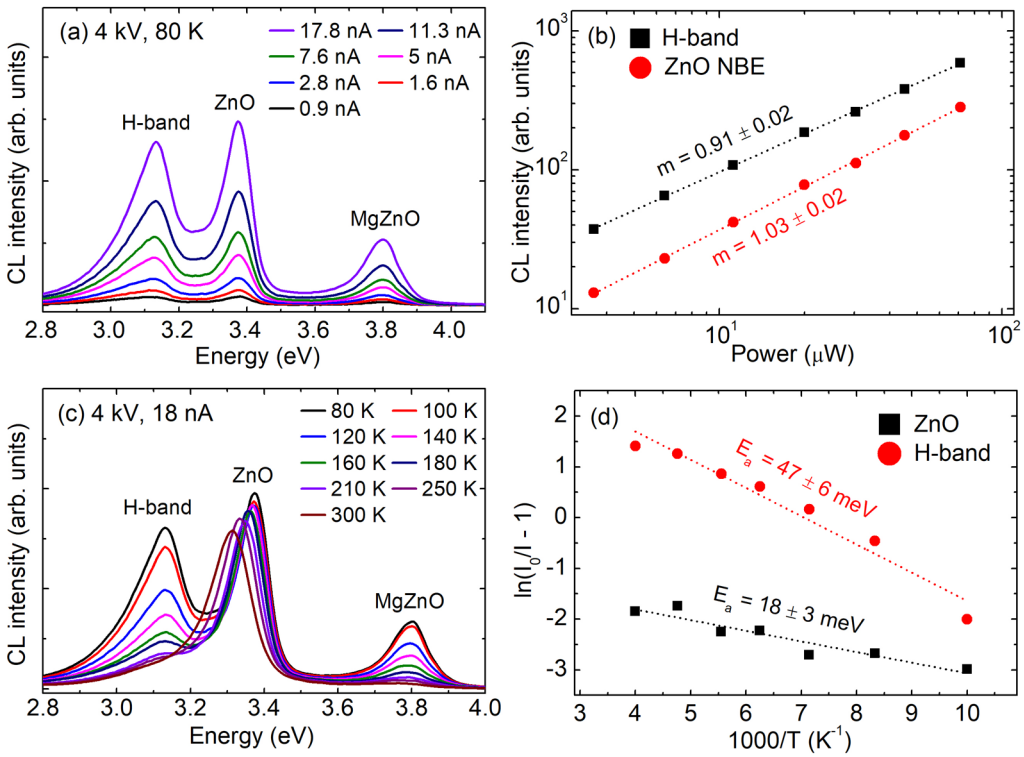


FIG. 6. (a) Excitation power-dependent CL spectra for the MgZnO/ZnO/$a$-ZnO heterostructure ($V_B = 4$ kV, $I_B = 0.9$–17.8 nA). (d) Analysis of the integrated peak intensities of the $H$ band and ZnO NBE using the power-law model, showing almost linear dependencies on excitation power. (c) Temperature-resolved CL spectra for the MgZnO/ZnO/$a$-ZnO, showing the presence of the H-band emission at temperatures up to 250 K. (d) Activation energies of the $H$ band and ZnO NBE determined using the Arrhenius law: $E_a$($a$-ZnO) $= 18 \pm 3$ and $E_a$($H$ band) $= 47 \pm 6$ meV.

indicating the $H$ band is not associated with a lattice coupled defect.

Temperature-resolved CL studies were carried out to investigate the dynamics of excitonic and $H$-band recombination in the MgZnO/ZnO heterostructures. The temperature-resolved CL spectra, shown in Figs. 5(c) and 6(c), reveal that the ZnO and MgZnO NBE emissions broaden and progressively shift to lower energies with increasing temperature. The temperature-dependent peak positions of the $H$ band, ZnO NBE and MgZnO NBE emissions are shown in Fig. 5S of the Supplemental Material [24]. The MgZnO and ZnO peaks progressively shift to lower energies due to the band gap narrowing with increasing temperature, whereas, conversely, the $H$-band peak position exhibits a weak dependence on temperature. The $H$-band peak shifts with temperature at rates of $2.7 \times 10^{-2}$ and $4.1 \times 10^{-2}$ meV/K for the MgZnO/ZnO/$a$-ZnO and MgZnO/ZnO/$m$-ZnO heterojunctions, respectively. These rates are significantly smaller than the reported values of 0.23 meV/K for the $H$ band in GaAs/AlGaAs [31] and ~0.1 meV/K in $Al_xGa_{1-x}As$/GaAs [32]. The temperature shift of the $H$ band is less pronounced than that of the ZnO NBE emission, consistent with the notion that the $H$-band luminescence originates from confined electrons in the triangular potential well arising from the polarization discrepancy at the interface [3]. The $H$-band energy can be approximated as [33]

$$E_{\text{H-band}} = E_g - E_{e,\text{loc}} - E_{e,\text{hole}},$$

where $E_g$ is the ZnO band gap, $E_{e,\text{loc}}$ is the localization energy of electrons in the interface potential well, and $E_{e,\text{hole}}$ the binding energy of the hole. When temperature is increased, $E_{e,\text{loc}}$ decreases due to the screening of the band bending by thermally excited carriers [34], which explains the smaller $H$-band shift with temperature compared with the ZnO NBE peak (see Fig. 5S of the Supplemental Material [24]). When temperature increases from 80 to 300 K, all the heterostructure emissions decrease in intensity due to enhanced electron-LO phonon interactions, albeit at different rates. The activation energies of the ZnO NBE and $H$ band can be derived using the Arrhenius law as shown in Figs. 5(d) and 6(d), yielding $E_a = 18$ and 32 meV for the ZnO layer grown on the $a$- and $m$-ZnO substrates, respectively. These values are in accord with the range of reported activation energies for ZnO excitons [35]. The activation energy for the $H$ band is almost identical for the heterostructures on $a$- and $m$-ZnO crystals, $E_a = 47 \pm 6$ meV. This extraordinarily high $E_a$, compared with the heterostructures of AlGaN/GaN (10 meV) [33] and MgZnO/ZnO/sapphire (19 meV) [3], gives the $H$-band exciton in MgZnO/ZnO heterostructures high thermal stability and explains why excitonic emission is observed at temperatures up to 250 K.

## IV. CONCLUSIONS

Our results indicate two-dimensional confinement of excitons, and associated $H$-band emission at the heterointerface in nonpolar MgZnO/ZnO bilayers without the involvement of spontaneous polarization. Epitaxial growth of the heterostructures on the $a$- and $m$-plane ZnO substrates results in a compressively strained interfacial layer in MgZnO, which generates piezoelectric polarization at the MgZnO/ZnO interface. An excitonic emission peaked at 3.12 eV is observed in the nonpolar MgZnO/ZnO heterostructures and identified as the $H$-band signature of interface bound excitons. It is shown through depth-resolved CL analysis and simulations that the $H$-band emission originates from the self-absorption of the ZnO free exciton emission in the ZnO region below the MgZnO/ZnO interface. The interface excitons are found to be highly stable with a thermal activation energy of 47 meV. In the case of the MgZnO/ZnO/nonpolar ZnO crystal, the $H$-band emission, relative to the FX, is found to be strongest when free excitons in ZnO are generated within 120 nm from the interface; this value corresponds to the expected carrier recombination length in the ZnO epilayer. More broadly, the results in this paper indicate the presence of confined 2D excitons and bound charges at the interface of nonpolar heterostructures due to the piezoelectric effect, which must be included in the assessment of oxide devices based on nonpolar materials.

## ACKNOWLEDGMENTS

This work was supported under Australian Research Council (ARC) Discovery Project Funding Scheme (Project No. DP210101146) and the Australian Academy of Technological Sciences and Engineering (ATSE) through the Global Connection Fund. M.Z. acknowledges financial support from the Australian Government through the Research Training Program Scholarship.

[1] R. Chaudhuri, S. J. Bader, Z. Chen, D. A. Muller, H. G. Xing, and D. Jena, Science **365**, 1454 (2019).

[2] A. Tsukazaki, S. Akasaka, K. Nakahara, Y. Ohno, H. Ohno, D. Maryenko, A. Ohtomo, and M. Kawasaki, Nat. Mater. **9**, 889 (2010).

[3] S. Choi, D. J. Rogers, E. V. Sandana, P. Bove, F. H. Teherani, C. Nenstiel, A. Hoffmann, R. McClintock, M. Razeghi, D. Look, A. Gentle, M. R. Phillips, and C. Ton-That, Sci. Rep. **7**, 7457 (2017).

[4] D. Q. Ye, Z. X. Mei, H. L. Liang, J. Q. Li, Y. N. Hou, C. Z. Gu, A. Azarov, A. Kuznetsov, W. C. Hong, Y. C. Lu, and X. L. Du, J. Phys. D: Appl. Phys. **47**, 255101 (2014).

[5] Y. Noel, C. M. Zicovich-Wilson, B. Civalleri, P. D'Arco, and R. Dovesi, Phys. Rev. B **65**, 014111 (2001).

[6] H. Tampo, K. Matsubara, A. Yamada, H. Shibata, P. Fons, M. Yamagata, H. Kanie, and S. Niki, J. Cryst. Growth **301**, 358 (2007).

[7] H. Y. Hwang, Y. Iwasa, M. Kawasaki, B. Keimer, N. Nagaosa, and Y. Tokura, Nat. Mater. **11**, 103 (2012).

[8] Y. Kozuka, A. Tsukazaki, and M. Kawasaki, Appl. Phys. Rev. **1**, 011303 (2014).

[9] X. L. Du, Z. X. Mei, Z. L. Liu, Y. Guo, T. C. Zhang, Y. N. Hou, Z. Zhang, Q. K. Xue, and A. Y. Kuznetsov, Adv. Mater. **21**, 4625 (2009).

[10] C. Morhain, T. Bretagnon, P. Lefebvre, X. Tang, P. Valvin, T. Guillet, B. Gil, T. Taliercio, M. Teisseire-Doninelli, B. Vinter, and C. Deparis, Phys. Rev. B **72**, 241305(R) (2005).
[11] G. Tabares, A. Hierro, M. Lopez-Ponce, E. Munoz, B. Vinter, and J. M. Chauveau, Appl. Phys. Lett. **106**, 061114 (2015).
[12] J. M. Chauveau, M. Teisseire, H. Kim-Chauveau, C. Deparis, C. Morhain, and B. Vinter, Appl. Phys. Lett. **97**, 081903 (2010).
[13] L. Beaur, T. Bretagnon, B. Gil, A. Kavokin, T. Guillet, C. Brimont, D. Tainoff, M. Teisseire, and J. M. Chauveau, Phys. Rev. B **84**, 165312 (2011).
[14] Y. C. Wu, J. H. Lin, W. R. Liu, and W. F. Hsieh, Appl. Surf. Sci. **537**, 147811 (2021).
[15] F. J. Klupfel, H. von Wenckstern, and M. Grundmann, Appl. Phys. Lett. **106**, 033502 (2015).
[16] P. R. Willmott and J. R. Huber, Rev. Mod. Phys. **72**, 315 (2000).
[17] N. Li, E.-H. Park, Y. Huang, S. Wang, A. Valencia, B. Nemeth, J. Nause, and I. Ferguson, Proc. SPIE **6337**, 63370Z (2006).
[18] K. Maeda, M. Sato, I. Niikura, and T. Fukuda, Semicond. Sci. Technol. **20**, S49 (2005).
[19] M. Zakria, P. Bove, D. J. Rogers, F. H. Teherani, E. V. Sandana, M. R. Phillips, and C. Ton-That, J. Mater. Chem. C **8**, 6435 (2020).
[20] C. Ton-That and M. R. Phillips, in *Semiconductor Nanowires: Materials, Synthesis, Characterization and Applications*, edited by J. Arbiol, and Q. Xiong (Woodhead, Cambridge, UK, 2015), p. 393.
[21] O. Dulub, L. A. Boatner, and U. Diebold, Surf. Sci. **519**, 201 (2002).
[22] J. Zippel, M. Lorenz, M. Lange, M. Stolzel, G. Benndorf, and M. Grundmann, J. Cryst. Growth **364**, 81 (2013).
[23] D. K. Hwang, K. P. Kim, and D. H. Kim, Thin. Solid Films **546**, 18 (2013).
[24] See Supplemental Material at http://link.aps.org/supplemental/10.1103/PhysRevMaterials.6.035202 for detailed characterization of the heterostructures.
[25] M. F. Romero, M. Feneberg, P. Moser, C. Berger, J. Blasing, A. Dadgar, A. Krost, E. Sakalauskas, and R. Goldhahn, Appl. Phys. Lett. **100**, 212101 (2012).
[26] G. D. Gilliland, D. J. Wolford, T. F. Kuech, and J. A. Bradley, Phys. Rev. B **43**, 14251 (1991).
[27] J. Liu, C. Shan, S. Wang, B. Li, Z. Zhang, and D. Shen, J. Cryst. Growth **347**, 95 (2012).
[28] S. H. Park and D. Ahn, Appl. Phys. Lett. **87**, 253509 (2005).
[29] D. Drouin, P. Hovington, and R. Gauvin, Scanning **19**, 20 (1997).
[30] C. Ton-That, L. Weston, and M. R. Phillips, Phys. Rev. B **86**, 115205 (2012).
[31] Y. R. Yuan, M. A. A. Pudenzi, G. A. Vawter, and J. L. Merz, J. Appl. Phys. **58**, 397 (1985).
[32] D. C. Reynolds, D. C. Look, B. Jogai, P. W. Yu, K. Evans, C. E. Stutz, and L. Radomsky, Phys. Rev. B **50**, 7461 (1994).
[33] G. Martinez-Criado, C. Miskys, U. Karrer, O. Ambacher, and M. Stutzmann, Jpn. J. Appl. Phys., Part 1 **43**, 3360 (2004).
[34] H. Chen, S. L. Gu, J. G. Liu, J. D. Ye, K. Tang, S. M. Zhu, and Y. D. Zheng, Appl. Phys. Lett. **99**, 211906 (2011).
[35] M. R. Wagner, G. Callsen, J. S. Reparaz, J.-H. Schulze, R. Kirste, M. Cobet, I. A. Ostapenko, S. Rodt, C. Nenstiel, M. Kaiser, A. Hoffmann, A. V. Rodina, M. R. Phillips, S. Lautenschläger, S. Eisermann, and B. K. Meyer, Phys. Rev. B **84**, 035313 (2011).